X-ray magnetic circular dichroism imaging with hard X-rays

K. Sato,[a]* Y. Ueji,[a] K. Okitsu,[a] T. Matsushita[b] and Y. Amemiya[a,c]

[a]Department of Applied Physics, The University of Tokyo, Hongo, Bunkyo-ku, Tokyo 113-8656, Japan, [b]Institute of Materials Structure Science, High Energy Accelerator Research Organization (KEK), 1-1 Oho, Tsukuba, Ibaraki 305-0801, Japan, and [c]Department of Advanced Materials Science, The University of Tokyo, Hongo, Bunkyo-ku, Tokyo 113-8656, Japan. E-mail: sato@kohsai.t.u-tokyo.ac.jp

X-ray polarization-contrast images resulting from X-ray magnetic circular dichroism (XMCD) in the hard X-ray region have been successfully recorded for the first time. The apparatus used consisted of an X-ray polarizer, double X-ray phase retarders, and a high-spatial-resolution X-ray charge-coupled-device detector. The sample used was a hexagonal-close-packed cobalt polycrystal foil having a thickness of about 4 μm. The X-ray polarization-contrast image resulting from XMCD was observed at a photon energy of 10 eV above the cobalt K-absorption edge (7709 eV). The observed contrast in the image was reversed by inversion of the magnetic field. Furthermore, the contrast was reversed again at a photon energy of 32 eV above the cobalt K-absorption edge.

1. Introduction

Magneto-optical effects in the X-ray spectral range have been receiving considerable interest because they provide information on the magnetic and electronic properties of materials. In particular, a spectroscopic technique, reflecting X-ray magnetic circular dichroism (XMCD), in core-level absorption is now a most popular magnetic effect, because it is sensitive to element-specific orbital- and spin-magnetic moments. With this technique, the localized and itinerant magnetisms, which give rise to a wide range of magnetic properties, are revealed in many cases in both theoretical and experimental aspects (Tischer *et al.*, 1995; Strange & Gyorffy, 1995; Guo, 1997). Nevertheless, the information obtained from the XMCD spectra is limited to that averaged spatially over the sample area where X-rays impinge, though the magnetic properties are dominated by the magnetic domains. Hence, microscopic observation of the spatial distribution of the XMCD in magnetic materials is of great significance.

In the soft X-ray region (less than 1 keV), several kinds of XMCD microscopy have been reported. Stöhr *et al.* (1993) have observed magnetic domains in a magnetic recording disc by employing a photoelectron emission microscope (PEEM) with XMCD. Kagoshima *et al.* (1996) have observed them in a nickel-based video tape with a 1 μm spot of circularly polarized undulator radiation, employing a scanning X-ray microscope (SXM). Fischer *et al.* (1996, 1999) have observed them in a layered Gd–Fe system, using a XMCD and a transmission X-ray microscope (TXM) system composed of a Fresnel zone plate and a high-resolution CCD detector. Hillebrecht *et*

al. (1995) have observed them in an Fe (100) single crystal with photoemission microscopy by utilizing X-ray magnetic linear dichroism (XMLD). In the hard X-ray region (above 1 keV), however, XMCD (XMLD) microscopy has not been reported so far.

Owing to direct observations of the electronic transitions in 3d transition metals (TMs), 4f rare-earth metals (RMs), and 5f TMs, the signals arising from XMCD are considerably large in the soft X-ray region (of the order of 10%) in comparison with those in the hard X-ray region (<1%). Thus, emphasis has been placed on the soft X-ray region in XMCD experiments. Many kinds of absorption edges, such as the K-absorption edges in 3d TMs, the L-absorption edges in 4f RMs, and 5f TMs, however, exist in the hard X-ray spectral range of ∼6–12 keV. From this viewpoint, one may say that XMCD with hard X-rays offers an opportunity to probe the magnetism as well as that with soft X-rays. As one of the examples, recent studies of magnetism have been focused on the TM K-absorption edges in the RM–TM intermetallics, in which a surprising variety of magnetic behaviours (Chaboy *et al.*, 1998; Rueff *et al.*, 1999; Garcia *et al.*, 2000) are indicated. In addition, magnetic materials naturally possess structures in the direction of the penetration depth of X-rays in the respective magnetic domains, namely three-dimensional structures from the surface to the bulk. If tomography techniques are employed, the large penetration depth of hard X-rays would allow one to observe an inner three-dimensional polarization-sensitive structure of the magnetic materials. Also, experiments with hard X-rays can be performed in easier circumstances, *e.g.* under atmospheric conditions. Hence, when the XMCD microscopy is extended to the hard X-ray spectral range, it can be a powerful tool for studies of various magnetic materials containing the above-mentioned atoms.

There are three ways to obtain circularly polarized X-rays from synchrotron radiation. The first is to use off-axis synchrotron X-ray radiation, *i.e.* right- and left-circularly polarized X-rays viewed from above and below a plane of the electron orbit of a storage ring (Schütz *et al.*, 1987). The degree of polarization obtained with this arrangement, however, was as low as 90% even at the expense of the X-ray intensity (85%). Furthermore, a non-uniformity in the intensity across the incident X-ray beam causes an inevitable difficulty when we extract the polarization-contrast images from the raw images. The second way is to use circularly polarized X-rays emitted from an insertion device (Yamamoto & Kitamura, 1987; Goulon *et al.*, 1998). Generally, X-ray beams from high-brilliance synchrotron sources with insertion devices are used in combination with monochromators. As a result, the degrees of the polarization of the X-ray beams deteriorate (∼70%). The third way is to use a polarization-switching technique with a phase retarder. This technique can produce an extremely high degree of X-ray polarization (>>95%), and is quite promising for extracting the small polarization contrast arising from XMCD.

We have developed a polarization-switching X-ray optics with a double X-ray phase-retarder system (Okitsu *et al.*, 2001*a*), which compensates for off-axis aberration. Alternatively, a quadruple X-ray phase-retarder system can be employed (Okitsu *et al.*, 2001*b*), which compensates for both off-axis and chromatic aberrations. In addition, we have developed a high-spatial-resolution X-ray CCD imaging system (Sato, Hasegawa *et al.*, 2000). Recently, we have demonstrated an X-ray natural linear dichroism (XNLD) with hard X-rays by combining the polarization-switching X-ray optics and the high-spatial-resolution X-ray CCD imaging system (Sato, Okitsu *et al.*, 2000). In this paper, we will report on the first observation of X-ray polarization-contrast images arising from the XMCD in the hard X-ray spectral range.
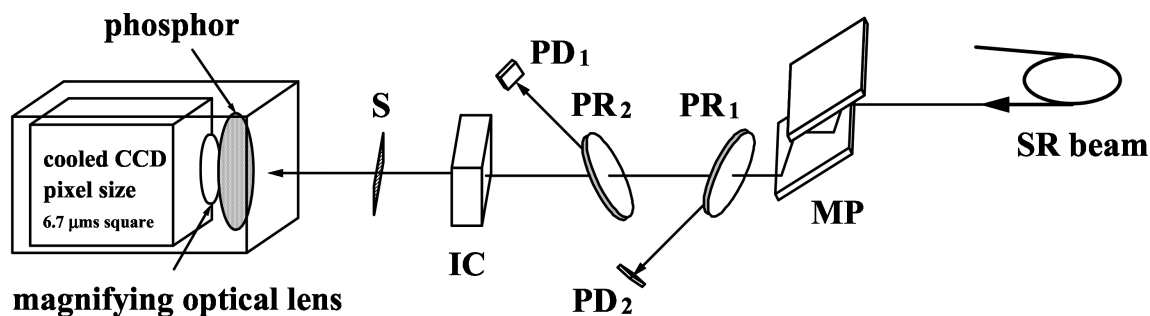
2. Experimental

Experiments were performed at BL-15C at the Photon Factory (KEK). The experimental set-up is schematically shown in Fig. 1. It consisted of a polarization-switching X-ray optics and a high-spatial-resolution CCD detector (Sato, Hasegawa *et al.*, 2000). The former was composed of a silicon 422 channel-cut offset X-ray polarizer (P) and diamond 111 double phase retarders (PR$_1$ and PR$_2$) (Okitsu *et al.*, 2001a). The synchrotron white X-ray beam (SR beam) was monochromated and horizontally polarized at X-ray energies near the cobalt K-absorption edge (7709 eV). The monochromated and horizontally polarized X-rays were incident to the double phase retarders mentioned previously. By adjusting the double phase retarders carefully, the polarization state of the transmitted X-rays could be switched between right- and left-circular polarization (looking towards the source) with high degrees of polarization (>>95%) at a rate of 0.3 Hz. The transmissivity of the double phase retarders was 35% at the cobalt K-absorption edge. The circularly polarized X-rays transmitted by the sample (S) were incident on a CCD detector. The X-ray CCD detector consisted of a phosphor screen, a magnifying optical lens, and a CCD. Gd$_2$O$_2$S:Tb (P-43) sedimented to a thickness of 6 μm on a beryllium plate was used as a phosphor screen. The magnification factor of the magnifying optical lens was fixed at ×10. The X-ray images were converted to visible-light images by the phosphor screen. The visible-light images were magnified with the magnifying optical lens and recorded on the CCD. The images were taken with an integration time of about 30 h. The performance characteristics of this X-ray CCD detector system are presented in detail elsewhere (Sato, Hasegawa *et al.*, 2000). The spatial resolution of the imaging system was evaluated to be 5.3 μm by a knife-edge technique. We also tested a phosphor screen of YAG:Ce, and obtained a spatial resolution of 3.6 μm (Sato, Hasegawa *et al.*, 2000). The conversion gain of this phosphor screen, however, was lower than that with the Gd$_2$O$_2$S:Tb (P-43). We thus decided to use the Gd$_2$O$_2$S:Tb (P-43) as a phosphor screen from the viewpoint of a compromise between the spatial resolution and the efficiency.

Before conducting experiments of XMCD imaging, we measured the XMCD spectrum of a sample at X-ray energies in the vicinity of the cobalt K-absorption edge (7709 eV). The sample used was a 4 μm-thick hexagonal-close-packed (h.c.p.) cobalt polycrystal foil. It was magnetized with an electromagnet, the magnetic field of which was 793 G, and was fixed in the direction of 45° tilted from the direction of the incident beam. The direction of the magnetic field was horizontal along the surface of the sample. An energy scan was performed by changing the Bragg-reflection angle of the X-ray polarizer with an energy step of about 1.5 eV. Data were accumulated for a preset time of 10–40 s, and the measurements were repeated five times for each spectrum so that the statistical errors were improved. Two XMCD spectra were measured under two opposite directions of the magnetic field. The measured XMCD spectrum exhibited the largest negative and positive peaks at photon energies of 7719 eV and 7741 eV (10 eV and 32 eV above the cobalt K-absorption edge) as a result of the XMCD effect (described in detail in §3). Therefore, we decided to use X-ray energies of 10 eV and 32 eV above the cobalt K-absorption edge for the XMCD imaging experiment, so that the maximum polarization-contrasts arising from XMCD would be observed in the image.

For the XMCD imaging experiments, the sample used in the above-mentioned experiments was divided into two pieces, which were placed so that the X-ray beam would be incident to respective pieces at angles of +45 and −45° from the surfaces. A schematic arrangement of the sample viewed from above is illustrated in Fig. 2. The sample was magnetized under a 793 G magnetic field with an electromagnet. The direction of the magnetic field made angles of +45 and −45° from the surfaces of the sample. The photon spin direction of the circularly polarized X-rays and the magnetization direction were parallel in one area and anti-parallel in another area. We refer to these areas as area 1 and area 2, which were aligned in the CCD field of view of 686 μm × 858 μm.

The images recorded on the CCD were normalized by integrated values of an ion chamber (IC) placed upstream of the sample, after the dark current of the CCD detector was subtracted. Absorption contrast images, $(\mu t)_r(\mathbf{r})$ and $(\mu t)_l(\mathbf{r})$, were obtained from the

High resolution X-ray CCD Detector
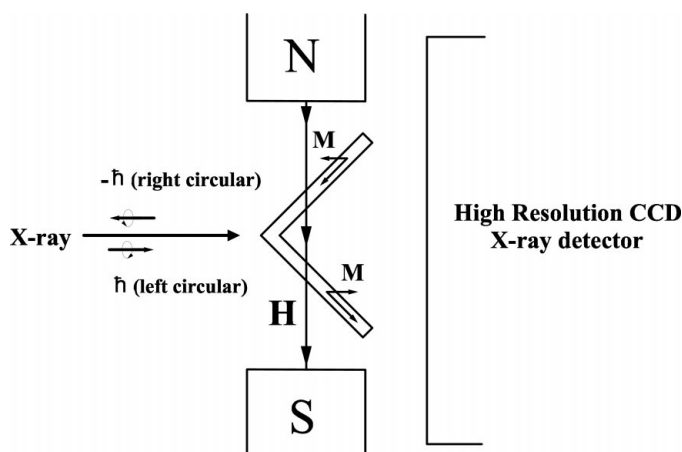
Figure 1
Experimental set-up for acquiring images resulting from X-ray dichroism. MP: silicon 422 monochromating polarizer. PR$_1$ and PR$_2$: first and second diamond 111 phase retarders. PD$_1$: PIN photodiode monitoring X-rays reflected by the first phase retarder. PD$_2$: PIN photodiode monitoring X-rays reflected by the second phase retarder. IC: ionization chamber monitoring X-rays incident to the sample. S: sample. SR: synchrotron radiation.

normalized images with and without the sample for both right- and left-circularly polarized X-rays, respectively. We now assume that the polarization-independent absorption coefficient ($\bar{\mu}$) is equivalent to the average of the absorption coefficients for opposite-handed polarization (μ_r, μ_l),

$$\bar{\mu} = \frac{\mu_r + \mu_l}{2}. \qquad (1)$$

Then, the image of the polarization-independent absorption is written as

$$\bar{\mu} t(\mathbf{r}) = \frac{(\mu t)_r(\mathbf{r}) + (\mu t)_l(\mathbf{r})}{2}, \qquad (2)$$

Figure 2
Schematic arrangement at the sample viewed from above. H, magnetic field; M, magnetic moment.

where $t(\mathbf{r})$ is the two-dimensional distribution of the sample thickness. Thus, by using the value of $\bar{\mu}$ measured by the spectroscopic experiment, we can obtain $t(\mathbf{r})$ as

$$t(\mathbf{r}) = \frac{1}{\bar{\mu}} \frac{(\mu t)_r(\mathbf{r}) + (\mu t)_l(\mathbf{r})}{2}. \qquad (3)$$

The images of the absorption coefficient for both polarizations [$\mu_r(\mathbf{r})$, $\mu_l(\mathbf{r})$] are then written as

$$\mu_r(\mathbf{r}) = \frac{(\mu t)_r(\mathbf{r})}{t(\mathbf{r})} \qquad (4)$$

and

$$\mu_l(\mathbf{r}) = \frac{(\mu t)_l(\mathbf{r})}{t(\mathbf{r})}. \qquad (5)$$

Hence, we can obtain the polarization-contrast image [MCD($\mathbf{r}$)] as follows,

$$\mathrm{MCD}(\mathbf{r}) = \frac{\Delta\mu(\mathbf{r})}{\bar{\mu}(\mathbf{r})}$$

$$= \frac{\mu_r(\mathbf{r}) - \mu_l(\mathbf{r})}{\mu_r(\mathbf{r}) + \mu_l(\mathbf{r})}. \qquad (6)$$

Finally, a 10 × 10 binning was made in order to reduce the statistical fluctuation noise. The deterioration of the spatial resolution with this process is insignificant because the pixel size on an image (0.67 µm) is about one-tenth of the full width at half-maximum (FWHM) of the point spread function (5.3 µm).

3. Results and discussion

Fig. 3 shows the XMCD spectra (solid and dash-dot-dash lines) together with the absorption spectrum (dotted line). The origin of the
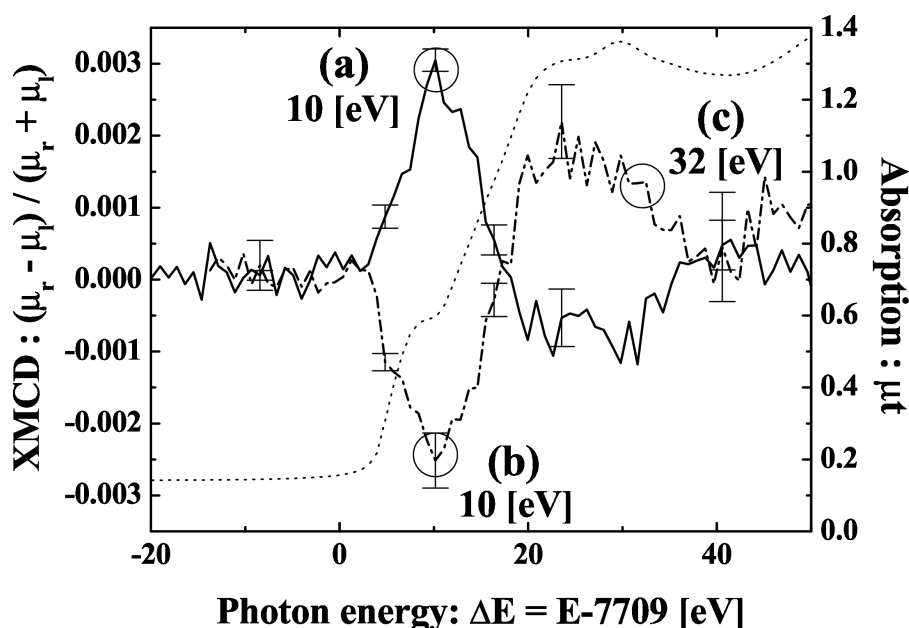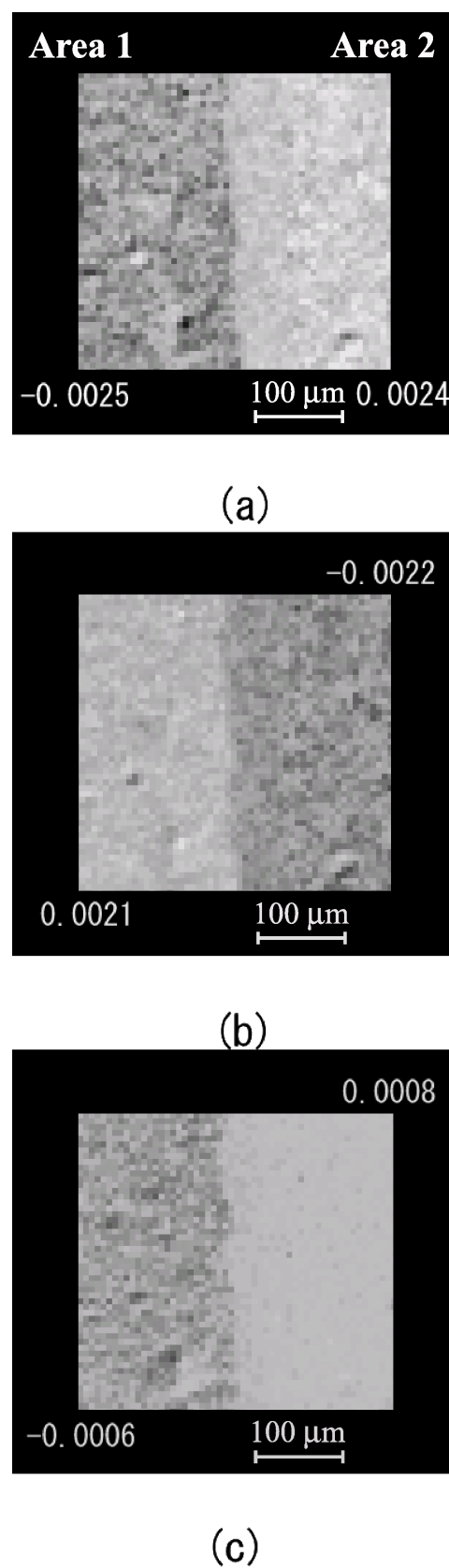

Figure 3
XMCD spectra (solid and dash-dot-dash lines) in an h.c.p. cobalt polycrystal along with its absorption spectrum (dotted line), measured with the double X-ray phase retarders. The directions of the magnetic field were parallel (solid line) and anti-parallel (dash-dot-dash line) to the X-ray photon spin direction of the right-circular polarization. Preset times were 10, 20, 30 and 40 s for −20 to −10, −10 to 0, 0 to 20 and 20 to 50 eV in the abscissa.

energy scale was selected at the edge jump of the absorption edge. The XMCD spectra (solid and dash-dot-dash lines) were recorded with opposite magnetic fields, parallel (solid line) and anti-parallel (dash-dot-dash line) to the X-ray photon spin direction of the right-circular polarization. These spectra were reversed by inverting the magnetic field, and exhibited the largest positive and negative peaks (±0.003 and ±0.001) at photon energies of 7119 eV and 7741 eV (10 eV and 32 eV above the cobalt K-absorption edge) as a result of the XMCD effect. The error bars in Fig. 3 were much larger in the energy range at about 20 eV. This feature is explained by increased statistical fluctuation of X-ray photons above the absorption edge. Their shapes and signs are in accordance with those previously found by other groups (Pizzini *et al.*, 1994; Rueff *et al.*, 1999). At the K-absorption edge ($1s \rightarrow 4p$) of TMs, despite intensive theoretical investigations based on both localized and itinerant pictures, no clear interpretation of the XMCD spectrum has yet been found. First (Thole *et al.*, 1992) and second (Carra *et al.*, 1993) sum rules can provide, in favourable cases, a separate determination of both the orbital and spin magnetic moments. This approach, however, fails at the TM K-absorption edges, where the excited electrons are promoted to the delocalized p states. Within multiple-scattering theory (Ebert *et al.*, 1988; Stähler *et al.*, 1993; Ankudinov & Rehr, 1995; Brouder *et al.*, 1996), Rueff *et al.* (1999) recently provided an explanation of the XMCD spectrum at the cobalt K-absorption edge in the h.c.p. cobalt, which was similar to that obtained in our work, by using semi-relativistic multiple-scattering theory. According to their analysis, this first peak in the XMCD spectra results from a well balanced mixing of three contributions, namely, the purely atomic contribution, the local contribution due to the spin polarization of the p-states on the absorbing site, and the contribution due to the scattering of the photoelectron by the spin-orbit potential of the neighbours and the absorber itself.

Fig. 4 shows the polarization-contrast images arising from the XMCD at 10 eV [(*a*) and (*b*) in Fig. 3] and 32 eV [(*c*) in Fig. 3] above the cobalt K-absorption edge after correction was made against the contrast resulting from the non-uniformity of the sample thickness. At a photon energy of 10 eV above the K-absorption edge [(*a*) in Fig. 3], area 1 and area 2 indicate darker and lighter greys, respectively (Fig. 4*a*). This means that the X-ray intensities are higher in area 1 than in area 2. The non-uniformities of the intensity observed in the respective areas are considered to result from residuals of the correction of the sample thickness. At the same photon energy [(*b*) in Fig. 3], the contrast in the image was reversed between area 1 and area 2 upon inverting the magnetic field (Fig. 4*b*). At a photon energy of 32 eV above the K-absorption edge [(*c*) in Fig. 3], the contrast in the image was reversed again between area 1 and area 2 (Fig. 4*c*).

In order to make a quantitative comparison, we calculated the XMCD values in the respective areas. The averaged pixel values in area 1 and area 2 in the XMCD image are -0.0025 and 0.0024, respectively, as shown in Fig. 4(*a*). These values are 0.0021 and -0.0022 in Fig. 4(*b*) and -0.0006 and 0.0008 in Fig. 4(*c*). All of the above values are consistent with those obtained from the XMCD spectra. Hence, it is concluded that these contrasts originate from differences in the magnetization directions of the sample, namely, originating from the effect of the XMCD in the h.c.p. cobalt polycrystal. The statistical fluctuations of the pixel values in the respective areas were ~ 0.0003. A discussion on the statistical fluctuation in the polarization-contrast image is presented in detail in our previous paper (Sato, Okitsu *et al.*, 2000).

Strictly speaking, however, there exist slight differences in the XMCD values between the images and the spectra. The XMCD values calculated from the images are slightly lower than those from

Figure 4
Images resulting from XMCD taken at 10 eV (*a*, *b*) and 32 eV (*c*) above the cobalt K-absorption edge (7709 eV) after correction for the non-uniformity of the sample thickness.

the spectra. These differences are attributed to different sample alignments in the XMCD imaging and spectroscopic experiments. As described in §2, the direction of the magnetic field was along the surface of the sample in the XMCD spectroscopic experiments, whereas it made angles of +45 and −45° from the surfaces of the sample in the XMCD imaging experiments. A magnetic field of 793 G is not sufficient to saturate the magnetization. It is thus expected that the XMCD effect is proportional to the magnitude of the magnetic field applied in the sample. The value of the XMCD (0.003) in the spectra (Fig. 3) was reduced to ∼71% (0.0024) in the image. This ratio coincides with that of the magnetic field (∼71%) in the spectroscopic and imaging experiments. Hence, the reduction of the XMCD values in the images can be explained reasonably, and it should be noticed that our measurements for both the spectroscopy and the imaging were achieved with high precision

Finally, we address the advantages and possible applications of this method. One of the advantages is element specificity, which results from the ability to tune the X-ray energies to the characteristic atomic absorption edges. In our polarization-switching X-ray optics, the nickel K-absorption edge (8333 eV) and the ion K-absorption edge (7111 eV) can be explored when silicon 511 and 331 are used, respectively, in addition to the cobalt K-absorption edge (7709 eV) with silicon 422. This suggests that this method is suitable for investigating various kinds of magnetic materials.

In addition, this method has some advantages when compared with the so-called Kerr microscopy, such as PEEM and SXM, in which photoelectrons are detected. PEEM has a high spatial resolution (∼20 nm), and samples to be observed do not need to be thinned. It does, however, have a critical disadvantage in that it cannot be operated in magnetic fields. SXM can be applied to thick samples in magnetic fields, but it takes a long time to record the magnetic images, even with highly intense X-rays. On the other hand, polarization-switching X-ray optics can record the XMCD images in magnetic fields, and the exposure time required for recording the images can be reduced in proportion to the X-ray intensity available.

Furthermore, the polarization-switching X-ray optics can be easily switched between circular and linear polarizations. Thus, this method can be applied to imaging arising from the XMLD in addition to XMCD under the same condition. As is well known, XMLD brings us the expectation value of the square of the magnetic moment, $\langle M^2 \rangle$, because of the sensitivity to the axis of M, whereas XMCD directly measures the magnetic moment, $\langle M \rangle$, *via* a transfer of the X-ray angular momentum vector in the absorption process. The information obtained from XMCD and XMLD are different, but correlative to each other. In principle, XMCD is suitable only for a unidirectional magnetic system, such as ferromagnets or ferrimagnets, while XMLD can be applied to all uniaxial magnetic systems, including antiferromagnets, as well. Hence, further information on the magnetism can be obtained by coupling XMCD and XMLD imagings.

4. Conclusions and outlook

We have developed a method for imaging the polarization contrasts arising from XMCD by combining a polarization-switching X-ray optics and a high-spatial-resolution CCD detector. With this method, XMCD images with about 0.3% and 0.1% contrasts at the cobalt K-absorption edge (7709 eV) have been clearly obtained from an h.c.p. cobalt polycrystal. The present study has demonstrated that XMCD imaging with hard X-rays is feasible, giving information on the direction of the magnetization with respect to that of the photon spin of the circular polarization. More generally, the technique should be applicable to studies of the magnetic domain structure of magnetic

materials. At the L-absorption edges in RE metals, much larger XMCD contrasts are expected. In the next step, this method will be applied to XMCD imaging at the L-absorption edges of RE systems, which are very important as magnetic systems. In this case, sum rules can be utilized for obtaining information on the spin and orbital moments separately. Also, this method will be applicable to studies of magnetic materials such as those used in video or audio tapes.

Furthermore, in order to improve the spatial resolution of this system, we plan to introduce a focusing optics and a Fresnel zone plate to magnify the XMCD image. This will improve the spatial resolution to 0.15 μm together with the use of a CCD camera having YAG:Ce as a phosphor screen (3.6 μm FWHM). In this case, the magnification factor of the Fresnel zone plate and the total length of the optical system are estimated to be ×20 and about 1 m, respectively. Regarding the required exposure time, it is expected to be reduced to 1/100, *i.e.* from 30 h to 20 min, when the experiments are performed at third-generation high-brilliance synchrotron radiation sources, such as SPring-8.

Although the amplitude of the XMCD signal with hard X-rays is lower than that with soft X-rays, the penetration depth of hard X-rays is larger than that of soft X-rays. By utilizing this characteristic, it is possible to employ tomography techniques in XMCD imaging with hard X-rays.

References

Ankudinov, A. & Rehr, J. J. (1995). *Phys. Rev. B*, **52**, 10214–10220.
Brouder, C., Alouani, M. & Bennemann, K. H. (1996). *Phys. Rev. B*, **54**, 7334–7349.
Carra, P., Thole, B. T., Altarelli, M. & Wang, X. (1993). *Phys. Rev. Lett.* **70**, 694–697.
Chaboy, J., García, L. M., Bartolomé, F., Maruyama, H., Marcelli, A. & Bozukov, L. (1998). *Phys. Rev. B*, **57**, 13386–13389.
Ebert, H., Strange, P. & Gyorffy, B. L. (1988). *Z. Phys. B*, **73**, 77–80.
Fischer, P., Eimüller, T., Kalchgruber, R., Schütz, G., Schmahl, G., Guttmann, P. & Bayreuther, G. (1999). *J. Synchrotron Rad.* **6**, 688–690.
Fischer, P., Schütz, G., Schmahl, G., Guttmann, P. & Raasch, D. (1996). *Z. Phys. B*, **101**, 313–316.
Garcia, F., Sampaio, L. C., Takeuchi, A. Y., Tolentino, H. & Fontaine, A. (2000). *J. Appl. Phys.* **87**, 5881–5883.
Goulon, J., Rogalev, A., Gauthier, C., Goulon-Ginet, C., Paste, S., Signorato, R., Neumann, C., Varga, L. & Malgrange, C. (1998). *J. Synchrotron Rad.* **5**, 232–238.
Guo, G. Y. (1997). *Phys. Rev. B*, **55**, 11619–11628.
Hillebrecht, F. U., Kinoshita, T., Spanke, D., Dresselhaus, J., Roth, Ch., Rose, H. B. & Kisker, E. (1995). *Phys. Rev. Lett.* **75**, 2224–2227.
Kagoshima, Y., Miura, T., Ando, M., Wang, J. & Aoki, S. (1996). *J. Appl. Phys.* **80**, 3124–3126.
Okitsu, K., Ueji, Y., Sato, K. & Amemiya, Y. (2001*a*). *J. Synchrotron Rad.* **8**, 33–37.
Okitsu, K., Ueji, Y., Sato, K. & Amemiya, Y. (2001*b*). In preparation.
Pizzini, S., Fontaine, A., Dartyge, E., Giorgetti, C., Baudelet, F., Kappler, J. P., Boher, P. & Giron, F. (1994). *Phys. Rev. B*, **50**, 3779–3788.
Rueff, J. P., Galéra, R. M., Giorgetti, C., Dartyge, E., Brouder, C. & Alouani, M. (1999). *Phys. Rev. B*, **58**, 12271–12281.
Sato, K., Hasegawa, Y., Kondo, K., Miyazaki, K., Matsushita, T. & Amemiya, Y. (2000). *Rev. Sci. Instrum.* **71**, 4449–4456.
Sato, K., Okitsu, K., Ueji, Y., Matsushita, T. & Amemiya, Y. (2000). *J. Synchrotron Rad.* **7**, 368–373.

Schütz, G., Wagner, W., Wilhelm, W., Kienle, P., Zeller, R., Frahm, R. & Materlik, G. (1987). *Phys. Rev. Lett.* **58**, 737–740.

Stähler, S., Schütz, G. & Ebert, H. (1993). *Phys. Rev. B*, **47**, 818–826.

Stöhr, J., Wu, Y., Hermsmeier, B. D., Samant, M. G., Harp, G. R., Koranda, S., Dunham, D. & Tonner, B. P. (1993). *Science*, **259**, 658–661.

Strange, P. & Gyorffy, B. L. (1995). *Phys. Rev. B*, **52**, R13091–13094.

Thole, B. T., Carra, P., Sette, F. & van der Laan, G. (1992). *Phys. Rev. Lett.* **68**, 1943–1946.

Tischer, M., Hjortstam, O., Arvanitis, D., Hunter Dunn, J., May, F., Baberschke, K., Trygg, J., Wills, J. M., Johansson, B. & Eriksson, O. (1995). *Phys. Rev. Lett.* **75**, 1602–1605.

Yamamoto, S. & Kitamura, H. (1987). *Jpn. J. Appl. Phys.* **26**, 1613–1615.